

# Coupled thermo-hydro-mechanical model for porous materials under frost action: theory and implementation

Zhen Liu · Xiong Yu

Received: 3 February 2011 / Accepted: 2 May 2011 / Published online: 15 May 2011  
© Springer-Verlag 2011

**Abstract** This paper introduces the development and implementation of a multiphysical model to simulate the coupled hydro-thermo-mechanical processes in freezing unsaturated porous materials. The model couples the Fourier's law for heat transfer, the generalized Richards' equation for fluid transfer in unsaturated media, and the mechanical constitutive relationship. Coupling parameters were defined to transfer information between field variables. Relationships, such as the similarity between drying and freezing processes and the Clapeyron equation for thermodynamic equilibrium during phase transition, were utilized to describe the effects of frost action. The coupled nonlinear partial differential equation system was solved under typical boundary conditions. The simulation results indicate that the model properly captured the coupling characteristics such as the thermally induced hydraulic and mechanical change in porous materials. Simulation was also conducted on an instrumented pavement section. The results of multiphysical simulations match reasonably well with the field-monitoring data.

**Keywords** Frost action · Hydro-thermo-mechanical model · Multiphysical model · Pavement · Unsaturated porous media

## 1 Introduction

Multiphysical processes are responsible for many interesting phenomena in unsaturated porous materials, e.g., hydro-diffusion and subsidence, drying and shrinkage, freezing and spalling, and capillarity and cracking [13]. There are generally two or more physical fields involved in these multiphysical processes. In some cases, the effects of coupling are not only noticeable but also critical. For example, the thermo-hydro-mechanical process can lead to noticeable stresses or deformations even without external loads. In many cases, multiphysics modeling is not only theoretically superior to solving individual unrelated processes but also practically necessary. The development of a sound multiphysics model requires understanding the fundamental mechanisms and the proper application of modeling techniques to obtain reliable simulation results.

The fundamental behaviors of porous materials under frost action have been investigated by means of experimental, analytical, or numerical approaches. Some research has focused on specific properties of porous materials, e.g., the hydraulic conductivity [18, 20, 32, 38, 56, 63], or the relationships between different parameters, e.g., the soil-water characteristic curve (SWCC, [19, 30, 37, 47, 52, 63]). Some other studies investigated the frost effects and the coupling mechanism [6, 7, 15, 21, 26, 46]. The forms of the governing equations for individual fields have also been investigated (i.e., [9, 10]).

The description of freezing porous materials inevitably involves more than one physical field, e.g., TH (thermo-hydraulic fields) or THM (thermo-hydro-mechanical fields) model. The development of modeling techniques for THM method has benefited from the advances in multiphysics research and simulation tools. For example, there are a substantial number of papers about the coupled thermo-

---

Paper presented at the International Workshop on Multiscale & Multiphysics Processes in Geomechanics, June 23–25, 2010, Stanford University.

---

Z. Liu · X. Yu (✉)  
Case Western Reserve University, Cleveland, OH, USA  
e-mail: xxy21@case.edu

hydro-mechanical (THM) model or thermo-hydro-mechanical-chemical model (THMC) for rocks and soils [2, 44, 49, 50, 58–62]. Noteworthy, these models were developed either from the non-isothermal consolidation of deformable porous media or from an extension to Biot's phenomenological model and generally did not consider the phase change of water (i.e., freezing/thawing phenomena) in porous media. They, however, can be extended to account for the effects of phase changes of water. The coupling models were usually solved by numerical method (finite difference (FD), finite element method (FEM), or finite volume (FV)) due to the highly nonlinear governing equations and complicated boundary conditions.

In conjunction with theoretical modeling efforts, tremendous amounts of work have been conducted to address practical issues in civil engineering, soil science, and agricultural engineering related to freezing porous materials, such as deterioration of geomaterials in frost regions. Questions raised from practice include the prediction of frost heave, the moisture and temperature redistribution, etc. Studies for addressing these issues usually led to TH or THM models, which can be categorized as rigid-ice models [35, 45, 54], thermodynamic models [22–24, 27, 28, 40, 42, 43], semi-empirical models [29, 41], and poromechanical models [13, 14].

The effects of freezing/thawing have been recognized as major factors causing the deteriorations of pavement structures in cold regions [55]. Both temperature and moisture content variations can pose significant environmental loads on pavement structure. Accurate prediction of pavement temperature from air temperatures will help pavement engineers to perform back-calculations of pavement moduli [67]. Moreover, the modulus of each pavement layer is also greatly affected by the moisture content, which significantly influences the pavement performance [68]. Moisture-induced damage of asphalt mixtures, referred as stripping, is one of the most detrimental factors affecting the in-service performance of asphalt pavements [11]. The ability to predict the temperature and moisture content distributions in a pavement will help to assess the performance of the pavement. For such purpose, several models have been proposed such as the Enhanced Integrative Climate Model (EICM) from The Federal Highway Administration. The limitations of EICM include (1) one-dimensionality and (2) neglecting the coupling effects of different fields. A few other coupled models have also been developed for this purpose [3, 53, 67]. The mechanical field, however, was not coupled in these models. Properly simulating the coupling effects on the mechanical and structural behaviors of pavement is essential for further advancing pavement research and practices.

This research aims to develop a coupled multiphysics simulation model to investigate the behaviors of porous materials under frost action. A theoretical framework is established to formulate the coupled thermo-hydro-

mechanical processes in freezing porous materials. The coupled model was solved numerically by finite element method. The performance of this model is validated by comparing simulation results with field data collected in an instrumented pavement. The simulation results predict typical phenomena observed in freezing unsaturated porous media, such as thermal-induced moisture migration, ice front development, and freezing-caused scaling of geomaterials. Furthermore, the model was applied to analyze an instrumented pavement. The simulation results closely match the field-monitoring data.

## 2 Theoretical basis

### 2.1 Thermal field

The thermal field is usually the main cause of multiphysical processes in freezing soils. For example, during the frost heave process, the sub-freezing temperatures cause the advancement of the frost front, which in return induces the fluid migration and soil deformation. This process produced by energy dissipation within the multiphase media can be alternatively explained as results of the varied surface tension, soil moisture suction, and kinetic energy changes associated with the hydrogen bond distribution, as well as thermally induced osmotic gradients [6, 7]. Besides the temperature-induced moisture flux or deformation, the energy carried by migratory fluid and the heat parameters influenced by fluid transport and metamorphic solid skeleton are also assumed as the 'reactions' to the temperature field. To precisely formulate energy transport in porous materials, a modified Fourier's equation with both conduction and convection terms (Eq. 1) was adopted.

$$C_a \frac{\partial T}{\partial t} = \nabla \cdot (\lambda \nabla T) - C_w \nabla \cdot (\mathbf{J}T) \quad (1)$$

where  $C_w$  is the heat capacity of unfrozen water,  $C_a$  is the apparent heat capacity,  $\lambda$  is the thermal conductivity,  $T$  is the temperature,  $t$  is time, and  $\mathbf{J}$  is the water flux from the hydraulic field. Both  $C_a$  and  $\lambda$  are coupling variables. The moisture migration changes the soil composition and consequently  $C_a$  and  $\lambda$ , which in turn affects the heat transfer process.

The effects of the air phase and radiation were neglected as the phase transition of water predominates in the process of energy conversion. The apparent volumetric heat capacity  $C_a$  in Eq. 1 takes into account the energy released/absorbed by the phase change of water. Instead of being treated as an energy sink or source on the right-hand side of the Fourier's equation, the enthalpy change due to the phase change can be incorporated into the heat capacity to reduce the nonlinearity [1].

$$C_a = C_s \theta_s + C_w \theta_w + C_i \theta_i + C_v (n - \theta_w - \theta_i) + L_f \frac{d\theta_i}{dt} \quad (2)$$

where  $\theta_s$ ,  $\theta_w$ , and  $\theta_i$  denote the volumetric content of soil mass, unfrozen water, and ice particles, respectively (the volume change of soil skeleton is neglected here). The same convention on subscripts applies to the other parameters.  $L_f$  is the latent heat.

The thermal conductivity  $\lambda$  in Eq. 1 can be approximated by empirical relationships such as in Eq. 3 [8, 23, 34]. There are also other similar relationships such as the equations proposed by Gardner [20], Sawada [51], and Campbell [5].

$$\lambda = C_1 + C_2(\theta_w + \theta_i F) - (C_1 - C_4) \cdot \exp\left\{-[C_3(\theta_w + \theta_i) + F\theta_i]^{C_5}\right\} \quad (3)$$

$$F = 1 + F_1\theta_i^{F_2} \quad (4)$$

where  $C_1$ ,  $C_2$ ,  $C_3$ ,  $C_4$ ,  $C_5$ ,  $F_1$ , and  $F_2$  are empirical curve-fitting constants.

## 2.2 Hydraulic field

For variably unsaturated porous media, the fluid movement is generally described by the mixed-type Richards' equation, which was shown to have good performance in ensuring mass conservation [9]. To extend the Richards' equation, a term related to ice formation needs to be added to the left-hand side of the Richards' equation to obtain Eq. 5.

$$\frac{\partial \theta_w}{\partial t} + \frac{\rho_i}{\rho_w} \frac{\partial \theta_i}{\partial t} = \nabla \cdot (K_{Lh} \nabla h + K_{Lh} \mathbf{i} + K_{LT} \nabla T) \quad (5)$$

where  $\theta_w$  is the volumetric content of water,  $\theta_i$  is the volumetric content of ice,  $\rho_w$  is the density of water,  $\rho_i$  is the density of ice,  $K_{Lh}$  is the hydraulic conductivity,  $K_{LT}$  is the hydraulic conductivity due to thermal gradient,  $\mathbf{i}$  is the unit vector along the direction of gravity, and  $h$  is the matric potential head (or pressure head). The matric potential head is the equivalent water head (unit: m) of the matric potential (unit: Pa). The two quantities are mathematically related via the unit weight of water. The concept of matric potential is used throughout this paper except for equations, where concept of the matric potential head is used.

Based on the analogy of freezing and drying processes, it has been accepted that the concept of the soil–water characteristic curve (SWCC) can be extended to describe the relationship between unfrozen water content and the matric potential (negative water suction) [30, 57]. The hydraulic conductivity can be estimated by integration of the SWCC [12, 18, 38]. This study employed either the simplified van Genuchten's equation ([23, 63], Eq. 6) or Fredlund's equation [19] when necessary data are available to describe the SWCC. Different approaches were then adopted to predict the hydraulic conductivity based on the SWCC.

$$S_e = \frac{\theta - \theta_r}{\theta_s - \theta_r} = (1 + |\alpha h|^n)^{-m} \quad (6)$$

where  $S_e$  is the effective saturation,  $\theta_s$  and  $\theta_r$  are the saturated and residual water content, respectively, and  $\alpha$ ,  $m$ , and  $n$  are empirical parameters.

$K_{Lh}$  and  $K_{LT}$  are hydraulic conductivities related to pore water head and temperature, respectively. One set of accepted relationships for these parameters are:

$$K_{Lh} = K_s S_e \left[ 1 - \left( 1 - S_e^{1/m} \right) \right]^2 \quad (7)$$

$$K_{LT} = K_{Lh} \left( h G_{wT} \frac{1}{\gamma_0} \frac{d\gamma}{dT} \right) \quad (8)$$

where  $\gamma$  denotes the surface tension of soil water, which is temperature dependent and can be approximated as  $\gamma = 75.6 - 0.1425T - 2.38 \times 10^{-4}T^2$ ;  $\gamma_0$  is the value of  $\gamma$  at 25°C, i.e.,  $\gamma_0 = 71.89 \times 10^{-3} \text{ kg m}^3$ .

As shown in Eq. 7, the hydraulic conductivity in partially saturated or partially frozen soil,  $K_{Lh}$  is obtained by multiplying the saturated conductivity with a saturation-dependent 'relative conductivity' term. The thermal-induced hydraulic conductivity in Eq. 8 was developed from the thermodynamics theory [46].  $G_{wT}$  is a gain factor, which has a value of around 7 for coarse-grained soils [45]. The dependence of viscosity on temperature was neglected here to unify the equations for the intrinsic hydraulic conductivity and the hydraulic conductivity.

The role of ice as an impedance for fluid migration was first proposed by Harlan [24] while studying the unsaturated hydraulic conductivity in partially frozen media. This viewpoint was confirmed by subsequent researchers such as Jame (1978) and Hansson et al. [23]. An impedance factor was adopted to describe the effects of ice on the fluid migration. However, a few pieces of recent research proposed that the impedance factor is unnecessary as long as the SWCC is precisely determined [39, 64].

When phase changes are involved, the generalized Clapeyron equation (Eq. 9) was used to describe the condition for the co-existence of water and ice. The local freezing point of pore fluid can be obtained from the generalized Clapeyron equation (Eq. 9).

$$\frac{dh}{dT} = \frac{L_f}{gT} \quad (9)$$

where  $h$  is the water head,  $L_f$  is the latent heat of water, and  $g$  is gravitational acceleration.

Assuming thermodynamic equilibrium conditions are maintained at the ice-pore/water interface at infinitesimal time intervals, the Clapeyron equation can be used to determine the ice content via Eq. 10.

$$\frac{d\theta_i}{dT} = \frac{L_f}{gT} \frac{d\theta}{dT} \quad (10)$$

### 3 The stress and strain field

The governing equation for the stress field is the Navier's equation, which incorporates the equation of motion, strain–displacement correlation, and the constitutive relationship. The equation of motion (Equation of equilibrium) is introduced in general tensor format as,

$$\nabla \cdot (\mathbf{C}\nabla\mathbf{u}) + \mathbf{F} = \rho\ddot{\mathbf{u}} \quad (\nabla \cdot (\mathbf{C}\nabla\mathbf{u}) + \mathbf{F} = 0) \quad (11)$$

where  $\mathbf{u}$  is the displacement vector,  $\mathbf{C}$  is the fourth-order tensor of material stiffness, and  $\mathbf{F}$  is the body force vector.

The strain–displacement equation is,

$$\boldsymbol{\varepsilon} = \frac{1}{2} [\nabla\mathbf{u} + (\nabla\mathbf{u})^T] \quad (12)$$

The constitutive equation is

$$\boldsymbol{\sigma} = \mathbf{C} : \boldsymbol{\varepsilon} \quad (13)$$

where,  $\boldsymbol{\sigma}$  is the Cauchy stress tensor,  $\boldsymbol{\varepsilon}$  is the infinitesimal strain tensor, and the symbol “:” stands for double contraction.

In order to consider the influence of the thermal field and the hydraulic field on the stress field, the constitutive relationship for porous materials has to be formulated as

$$\boldsymbol{\sigma} = \mathbf{D}\boldsymbol{\varepsilon}_{el} + \boldsymbol{\sigma}_0 \quad (14)$$

where  $\mathbf{D}$  is the stiffness matrix of soil skeleton,  $\boldsymbol{\sigma}_0$  is the initial stress vector, and  $\boldsymbol{\varepsilon}_{el}$  is the elastic strain that can be obtained from the following relationship

$$\boldsymbol{\varepsilon} = \boldsymbol{\varepsilon}_{el} + \boldsymbol{\varepsilon}_{th} + \boldsymbol{\varepsilon}_{tr} + \boldsymbol{\varepsilon}_{hp} + \boldsymbol{\varepsilon}_0 \quad (15)$$

where  $\boldsymbol{\varepsilon}_{th}$  is the strain caused by thermal expansion,  $[\alpha(T - T_{ref}), \alpha(T - T_{ref}), 0]^T$ ;  $\boldsymbol{\varepsilon}_{tr}$  is the strain caused by the phase change of water, which was approximated as  $[0.09Q, 0.09Q, 0]^T$  when a unit localization tensor in mixture theory is followed, where  $Q$  is the degree of water phase transition, and 0.09 is the relative change of volume when water turns into ice;  $\boldsymbol{\varepsilon}_0$  is the initial strain; and  $\boldsymbol{\varepsilon}_{hp}$  is the strain resulting from the change of the matric potential, which is calculated by  $[h/\mathbf{H}, h/\mathbf{H}, 0]^T$ .  $\mathbf{H}$  is a parameter similar to the modulus corresponding to matric potential. The value of  $\mathbf{H}$  can be obtained through experimental measurement. The use of  $\mathbf{H}$  casts light on the independent role of matric potential in the constitutive relationship of unsaturated porous media as indicated in Biot's model for unsaturated fluid with air bubble and in Fredlund's method to address volume change of unsaturated soil [4, 17].

### 3.1 General boundary condition

The general boundary condition, which includes the special cases such as the Dirichlet (first type), Neumann (second type), and Robin (third type) boundary conditions, was formulated by Eq. 16

$$\mathbf{n} \cdot (c\nabla u + \zeta u - \gamma) + qu = \delta - \mathbf{h}^T \boldsymbol{\mu} \quad (16)$$

where  $\mathbf{n}$  is the outward normal unit vector of a boundary,  $u$  is the dependent variable of individual field (temperature, matric potential, displacements, etc.),  $c$  is a conductivity term,  $\zeta$  is the conservative flux convection coefficient,  $\gamma$  is the source in the subdomain,  $q$  is the boundary absorption coefficient,  $\delta$  is the boundary source,  $\mathbf{h}^T$  is a matrix designated for the flexibility of the constraint type, and  $\boldsymbol{\mu}$  is the matrix of Lagrange multiplier.

## 4 Model implementation

The couplings of the three physical fields (i.e., hydraulic, thermal, and mechanical fields) were realized by means of variables and parameters that transfer information interactively. Due to the high nonlinearity, the equations have to be solved numerically. The coupled multiphysical model was solved with the assistance of COMSOL, a commercial multiphysics simulation platform. Firstly, the model geometries were constructed by the interactive graphic interface. The models were then customarily built, transformed into the weak form, and solved using the nonlinear solver provided by COMSOL. The results were analyzed using the post-processing functions provided by the software.

## 5 Simulation case I

Mizoguchi [36] conducted a classic benchmark experiment where four identical cylinder samples of 10 cm length and 8 cm height were packed with sandy loam. The initial temperature was 6.7°C, and volumetric water content was 0.33. The samples were thermally insulated in the sides and in the bottom. The top surface was exposed to a constant temperature of −7°C. After 12, 24, and 50 h, respectively, the samples were taken out and divided into 1-cm-thick slices to measure their water content distribution. The process was simulated by Hansson et al. [23] with a thermo-hydraulic algorithm. This experiment was chosen as the prototype for computational model construction in simulation case I.

A computational domain of 10 cm in length and 8 cm in height was used in the simulation. The initial temperature was 6.7°C, and volumetric water content was 0.33. The samples were thermally insulated (Neumann boundary condition, zero thermal gradient) in the sides and in the

bottom. The top surface was exposed to a constant temperature of  $-7^{\circ}\text{C}$ . The thermal boundary conditions are shown in Fig. 1. The heat influx in the surface was described by Newton’s law of cooling as Eq. 17

$$\mathbf{n} \cdot (\lambda \nabla T) = h_c (T_{\text{amb}} - T) \tag{17}$$

where  $\lambda$  is the thermal conductivity,  $h_c$  is the coefficient of convection heat transfer,  $T_{\text{amb}}$  is the ambient temperature, and  $T$  is the temperature at boundaries. All boundaries were hydraulic insulated (Neumann boundary condition, zero hydraulic gradient or no flow) to ensure mass conservation, which is mathematically described as

$$\mathbf{n} \cdot (K_{\text{Lh}} \nabla h + K_{\text{Lh}} \mathbf{i} + K_{\text{Lh}} \nabla T) = 0 \tag{18}$$

To implement the multiphysical simulation, the differential equations were first transformed into weak forms. Taking the Fourier’s equation for example, the weak form is

$$\begin{aligned} & \int_{\Omega} \left( \frac{\partial \theta}{\partial t} + \frac{\rho_i}{\rho_w} \frac{\partial \theta_i}{\partial t} \right) v dV \\ &= \int_{\partial \Omega} \mathbf{n} \cdot ((K_{\text{Lh}} \nabla h + K_{\text{Lh}} \mathbf{i} + K_{\text{Lh}} \nabla T) v) dS \\ &+ \int_{\partial \Omega} (K_{\text{Lh}} \nabla h + K_{\text{Lh}} \mathbf{i} + K_{\text{Lh}} \nabla T) \cdot \nabla v dV \end{aligned} \tag{19}$$

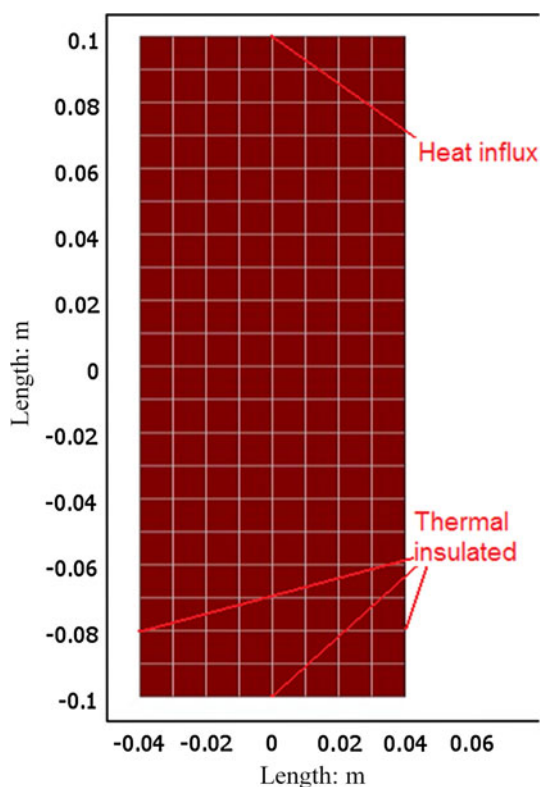


**Fig. 1** FEM mesh for the computational domain with thermal boundary conditions

where  $v$  is a nonnegative weighting function whose integration over domain  $\Omega$  equals 1.

Some soil parameters for the hydraulic field can be found in Hansson’s study [23]. Other parameters were set based on experimental data and related literature [17, 48]. The data are listed in Table 1.

The influence of ice content on the elastic moduli of soils is complicated. In this simulation, a simplified linear relationship was assumed between the ice content and the modulus of elasticity. This assumption was based on the experimental results on the effects of degree of freezing on the modulus of soils.

### 6 Results and analysis

The typical thermal properties, i.e., apparent heat capacity and thermal conductivity, are heavily dependent on the hydraulic field and the phase change of water. This dependence usually results in high nonlinearity that can significantly affect the multiphysical process. Plotted in Fig. 2 are the variations of the volumetric heat capacity and thermal conductivity with time at heights of 5, 10, 15, and 18 cm. It can be seen that the apparent heat capacity in Fig. 2a slightly decreases with time before temperature drops below the freezing point. This agrees with the fact that the water content decreased before ice starts to form. After icing starts, the progress of water turning into ice releases a considerable amount of heat that decelerates substantially the freezing process. This is equivalent to an increase in the apparent heat capacity. Therefore, the sudden increase in apparent heat capacity indicates the increasing contribution of latent heat of ice formation. The variation of the thermal conductivity follows a similar pattern, but demonstrating a less extent of nonlinearity.

The temperature distributions at different times are sketched in Fig. 3. Temperatures at all points drop as energy is extracted from the upper boundary. The overall rate of temperature change decreases as temperatures at some locales approach the freezing point. But it is worthwhile to point out that the freezing point of pore water is slightly lower than  $0^{\circ}\text{C}$ , a phenomena called freezing point depression. The depression of the freezing point of pore water refers to the difference between the local freezing point and the freezing point under standard atmospheric pressure ( $0^{\circ}\text{C}$ ). The extent of freezing point depression is determined by the pore size. Small pore produces large suction and consequently causes a larger amount of freezing point depression. The depressions of the freezing points in different locales are shown in Fig. 4. It is seen that the freezing point is not uniform throughout the computational region. But in fact, it turns out to be lower in

**Table 1** Constant parameters for simulation case I

Constant	Value	Units	Description
$h_c$	28	W/m <sup>2</sup> K	Convection heat transfer coefficient
$C_1$	0.55	W/m <sup>2</sup> K	Constant for thermal conductivity 1
$C_2$	0.8	W/m <sup>2</sup> K	Constant for thermal conductivity 2
$C_3$	3.07	W/m <sup>2</sup> K	Constant for thermal conductivity 3
$C_4$	0.13	W/m <sup>2</sup> K	Constant for thermal conductivity 4
$C_5$	4	1	Constant for thermal conductivity 5
$F_1$	13.05	1	Constant for thermal conductivity 6
$F_2$	1.06	1	Constant for thermal conductivity 7
$C_n$	$2 \times 10^{-6}$	J/m <sup>3</sup> K	Volumetric heat capacity of solid
$C_w$	$4.2 \times 10^{-6}$	J/m <sup>3</sup> K	Volumetric heat capacity of liquid
$C_v$	$1.2 \times 10^{-3}$	J/m <sup>3</sup> K	Volumetric heat capacity of vapor
$C_i$	$1.935 \times 10^{-6}$	J/m <sup>3</sup> K	Volumetric heat capacity of ice
$L_f$	$3.34 \times 10^{-5}$	J/kg	Latent heat of freezing or thawing of water
$\theta_0$	0.33	m <sup>3</sup> /m <sup>3</sup>	Initial water content
$\theta_r$	0.05	m <sup>3</sup> /m <sup>3</sup>	Residual water content
$\theta_s$	0.535	m <sup>3</sup> /m <sup>3</sup>	Saturated water content
$K_s$	$3.2 \times 10^{-6}$	m/s	Saturated hydraulic conductivity
$\alpha$	1.11	l/m	Empirical parameters 1 for hydraulic properties
$n$	1.48	1	Empirical parameters 2 for hydraulic properties
$m$	0.2	1	Empirical parameters 3 for hydraulic properties
$l$	0.5	1	Empirical parameters 4 for hydraulic properties
$\gamma_0$	71.89	g/s <sup>2</sup>	Surface tension of soil water at 25°C
$\rho_i$	931	kg/m <sup>3</sup>	Density of ice
$\rho_w$	1,000	kg/m <sup>3</sup>	Density of water
$\rho_n$	2,700	kg/m <sup>3</sup>	Density of soil solids
$T_0$	6.7	°C	Initial temperature
$T_{amb}$	−6	°C	Ambient temperature
$g$	9.8	m/s <sup>2</sup>	Gravitational acceleration
$\mu$	0.3	1	Poisson ratio
H	7,653	m	Modulus related to matric potential
al	$0.8 \times 10^{-6}$	1/K	Thermal expansion coefficient

layers adjacent to the upper boundary. Moreover, the freezing point continuously decreases versus time as freezing develops. The simulation results confirmed that there exists an obvious freezing point depression of water in porous media. The magnitude of the depression is dependent on the pore characteristics such as the pore size and the associated capillary action.

Accurate prediction of frost penetration, i.e., the depth of frost front, is essential for studying the frost action in porous media and is thus of great practical interest. In this study case, frost penetration can be plotted based on temperature variations in Fig. 3 and freezing point depression in Fig. 4. In comparison with the results predicted by an empirical equation [48], we found that the magnitude of the frost penetration predicted by the current model is greater than that calculated by the empirical equation (in Fig. 5). One possible reason for the difference is that the empirical

equation overlooks the influence of the hydraulic field and consequently the dramatic change on the thermal properties of soil. Therefore, the calculation with constant soil properties in the commonly used empirical equation may lead to a noticeable underestimation of the frost penetration depth.

Figure 6 plots the distribution of the total volumetric water content (the volumetric water content plus the volumetric ice content) at different times. The curves clearly demonstrate a trend that moisture migration moves toward the freezing front [29, 30]. This is consistent with commonly observed frost heave phenomena. Such phenomena have significant impacts on the pavement, foundations, and infrastructures. The total volumetric water content (including both in the liquid and solid state) is determined by both the temperature and matric potential. The unfrozen water content is determined by the water retention curve,

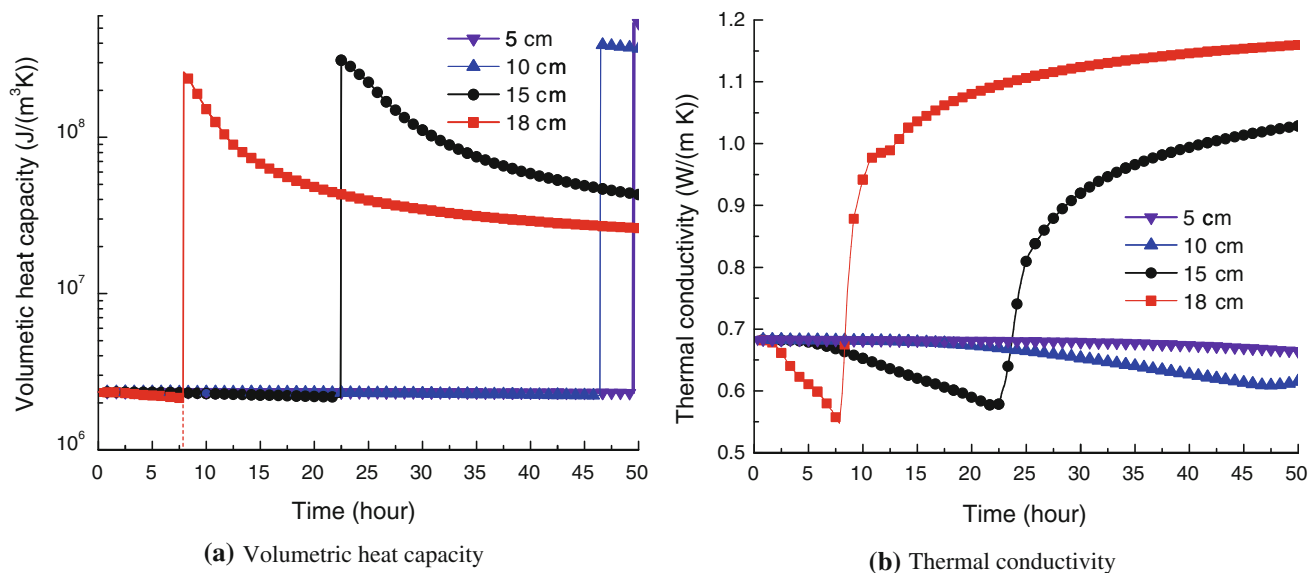


**Fig. 2** The variations of the thermal properties versus time

while the amount of ice is decided by the ice–water balance together with the mass balance. Temperature gradient is the driving factor for all the migration phenomena in this case. This is because the temperature gradient causes the hydraulic gradient, which then drives the moisture migration. When the matric potential satisfies the required temperature and pressure conditions for ice formation (described by the Clapeyron equation), water begins to turn into ice. In this model simulation, it was assumed that the water–ice balance is maintained in each infinitesimal time step. As shown in Fig. 6, the water content in the cold region (upper) of the model increases. At the same time, moisture from lower region migrates upward and gradually turns into ice.

The variation of ice distribution can also be predicted. As shown in Fig. 7, ice formed above the depth of frost penetration. The comparison of the ice content at 12, 24, and 50 h after freezing starts indicates that water continuously migrates into frozen area and turns into ice therein. The process is determined by both the thermodynamic equilibrium between ice and water and the water flow in the unsaturated porous media. The figure shows that at the beginning of freezing, the velocity of ice formation is very fast. The surface layer accumulates the greatest amount of ice.

Matric potential is essential to the mechanical properties of unsaturated porous materials, i.e., the shear strength of unsaturated soils (Vanapalli 1996). In this simulation, matric potential is a dependent variable of the hydraulic field that can be explicitly calculated. As shown in Fig. 8, the spatial distributions of matric potential head at different freezing times. The matric suction head, which is the negative of the matric potential head, is illustrated in Fig. 8. Its

magnitude is directly related to the liquid water content. It is shown that suction increases as liquid water content decreases, although the total ice and liquid water content may increase.

Figure 9 shows the variation of vertical deformation (or frost action) versus time. Given that the bottom of the sample was fixed, the vertical deformation can be determined from the average displacement on the top of the specimen. The volume changes as a result of the temperature change, the variation of matric potential, and the ice formation. The trend of volume change occurs in stages. In the 1st stage, the volume change is dominated by the thermal contraction of solids. However, the magnitude is negligible due to the small soil thermal expansion coefficient and the small range of temperature variation. The volume change is affected by two major phenomena in the 2nd stage, i.e., the volume contraction due to increase in matric potential and the volume expansion due to phase change (ice has around 10% larger specific volume than water). The increasing matric potential (as seen in Fig. 8) holds the particles tighter, leading to the amount of volume reduction counteracting the increases in the volume due to phase change of water. The trend of volume change from computational simulation implies that the effect of matric potential on volume change dominates over that by the phase change. This even caused volume contraction during certain period in the 2nd stage. In the 3rd stage, the volume continues to increase due to the volume increase associated with phase transition. The simulation is consistent with the experimental phenomena observed by Liu et al. [31].

Figure 10 shows the distribution of the vertical stress in the specimen due to freezing. The positive sign indicates tension. Both the maximum tensile and compressive

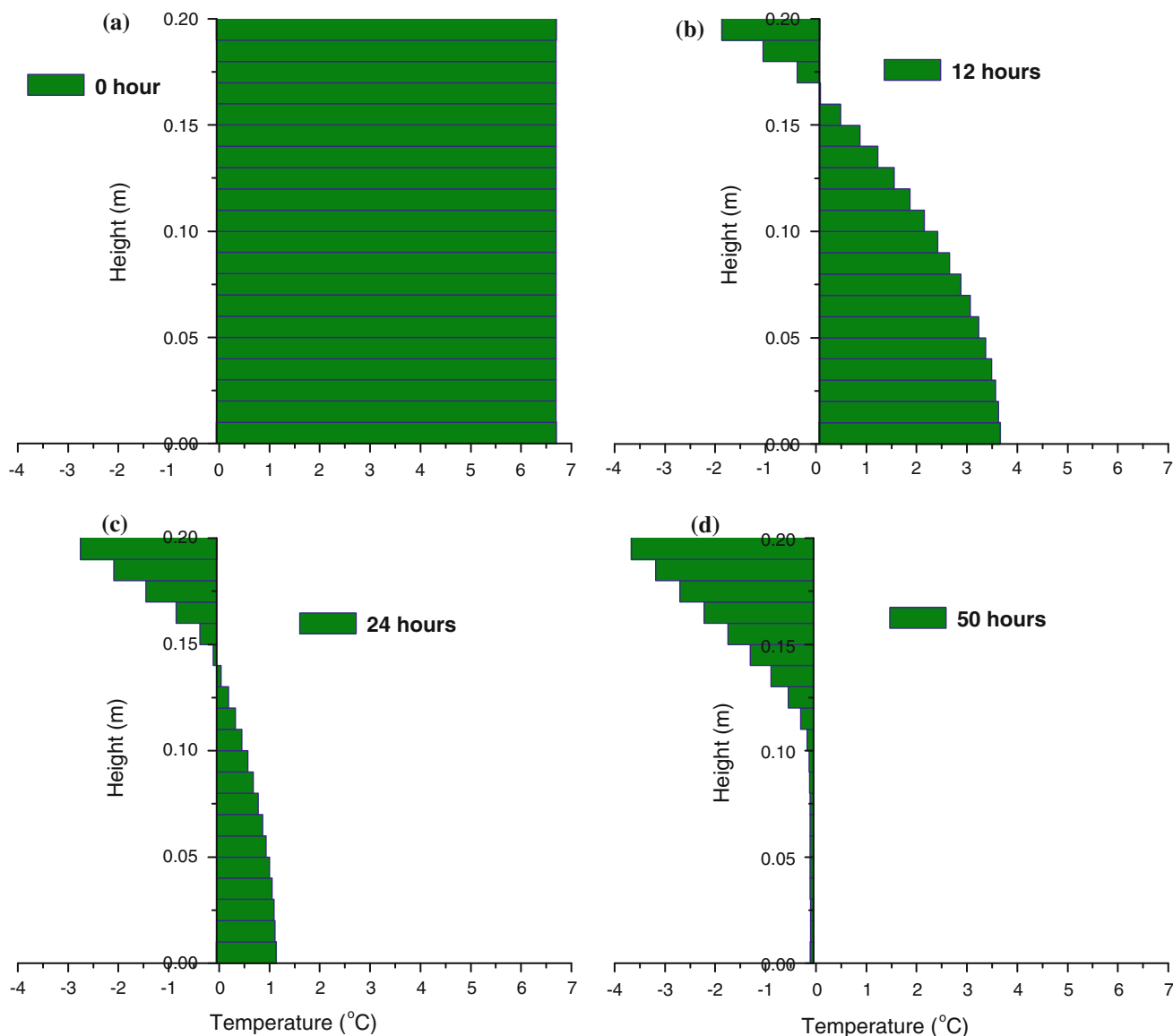


**Fig. 3** Temperature profile at different freezing times

stresses appear in the surface layer. The reason is that the moisture migrates and accumulates near the surface. The volume expansion due to ice crystallization leads to the internal stresses. It has been commonly observed that during thermal weathering of rocks in mountain areas, cracks typically appear first on the surface and then progresses to the interior. The stress distribution illustrated in Fig. 10 gives an explicit explanation on the fracture mechanism, since the high-tension and compression zones close to the surface are likely to initialize the formation of cracks. Besides, the simulation provides some insight into factors that control the crack spacing. However, the relationship between the thermal gradient, moisture gradient, internal stress, and crack spacing requires further investigations.

## 7 Simulation case: II

An instrumented road in Ohio, USA, was used as test bed to further validate the simulation model. The Ohio Department of Transportation launched a project in 1995 as a part of Strategic Highway Research Program (SHRP) Test Road [25, 33, 65]. A series of 34 instrumented pavement test sections were constructed on State Road 23 in Delaware County, Ohio, USA. The field sensors monitored the moisture content, resistivity, and frost depth as well as the air temperature. Additional information such as water table height is also available for sections that were originally designated for the assessment of seasonal effects on both Portland cement concrete pavement (rigid) and asphalt concrete pavement (flexible). Here, we selected

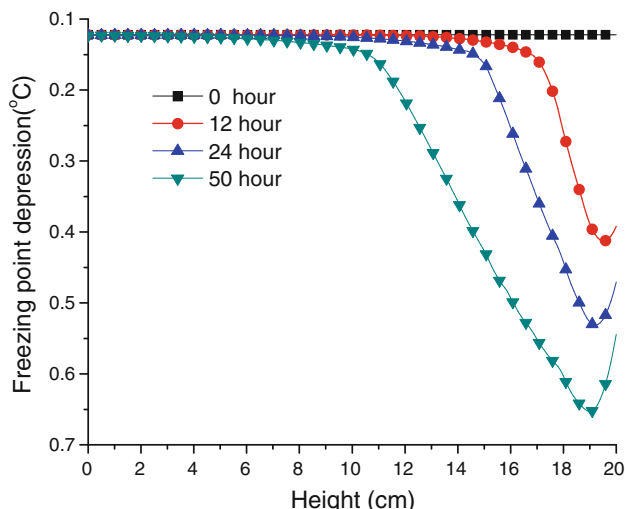


Fig. 4 Variation of freezing point depression along the depth at 0, 12, 24 and 50 h

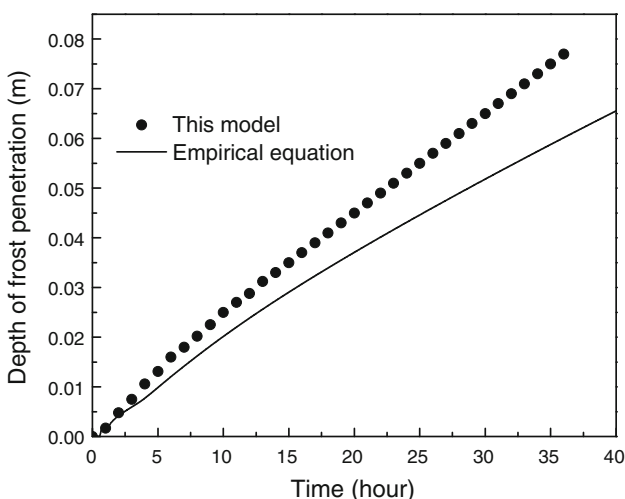


Fig. 5 The depths of frost penetration versus time

Section 390204 for the simulation study. The section consists of 11 inches of asphalt concrete pavement and 6 inches of aggregate base. Eighteen temperature gauges and 10 moisture gauges were installed within the pavement structure. Hourly air temperature and local soil temperature at each gauge were accessible. Moisture content information was available on the 1st, 9th, and 20th day. The period of simulation is between December 3 and December 22 in 1999.

### 7.1 Modeling

The computational domain, which is half of the pavement and embankment, is shown in Fig. 11. The geometry of the FEM model was constructed based on the real dimensions of the pavement structure and embankment. Tentative calculation was conducted to make sure the computational

domain is big enough to eliminate truncation effects on the simulation boundaries. Rectangular elements were employed in the FEM meshing.

Equations proposed by [18] was used to obtain the SWCCs of base and subgrade materials, i.e.,

$$\theta_w = C(h) \times \left\{ \frac{\theta_s}{\left[ \ln \left[ e + (9.8h/a)^b \right] \right]^c} \right\} \quad (20)$$

$$C(h) = \left[ 1 - \frac{\ln(1 + 9.8h/h_r)}{\ln(1 + 10^6/h_r)} \right] \quad (21)$$

where  $a$  is a parameter dependent on air entry value in kPa,  $b$  is a parameter dependent on the slope of SWCC curve after air entry value is exceeded,  $C$  is a parameter dependent on the suction at the residual water content, and  $h_r$  is a parameter dependent on the suction at the residual water content.

An empirical approach suggested by Zapata et al. [69] was adopted for the calculation of the parameters in the SWCC equation (Eqs. 20, 21). In this method, for a soil with plasticity index (PI) larger than 0, a parameter WPI is introduced, which is the product of PI and the ratio of soil passing ASTM No. 200 sieve (0.075 mm). The parameters were then estimated as:

$$a = 0.00364(WPI)^{3.35} + 4(WPI) + 11 \quad (22)$$

$$\frac{b}{c} = -2.313(WPI)^{0.14} + 5 \quad (23)$$

$$c = 0.514(WPI)^{0.465} + 0.5 \quad (24)$$

$$\frac{h_r}{a} = 32.44e^{0.0186WPI} \quad (25)$$

$$\theta_s = 0.0143(WPI)^{0.75} + 0.36 \quad (26)$$

The hydraulic conductivity was obtained through the relative permeability function integrated from the SWCC. The effect of temperature-dependent fluid viscosity was neglected for simplification.

$$k_r(h) = \frac{\int_{\ln(h)}^b \frac{\theta(e^y) - \theta(h)}{e^y} \theta'(e^y) dy}{\int_{\ln(h_{aev})}^b \frac{\theta(e^y) - \theta_s}{e^y} \theta'(e^y) dy} \quad (27)$$

where  $b$  is equal to  $\ln(1000000)$ ,  $y$  is a dummy variable of integration representing the logarithm of suction, and  $h_{aev}$  is the air entry value of matric potential head.

The WPI value for the field subgrade soils was obtained as 21.12 from experimental data on the dense-graded aggregate base and subgrade soil. The subgrade soil was classified as A6 soil by AASHTO specification. A computer code was developed to obtain the SWCCs and the relative permeabilities. The results are shown in Figs. 12 and 13.

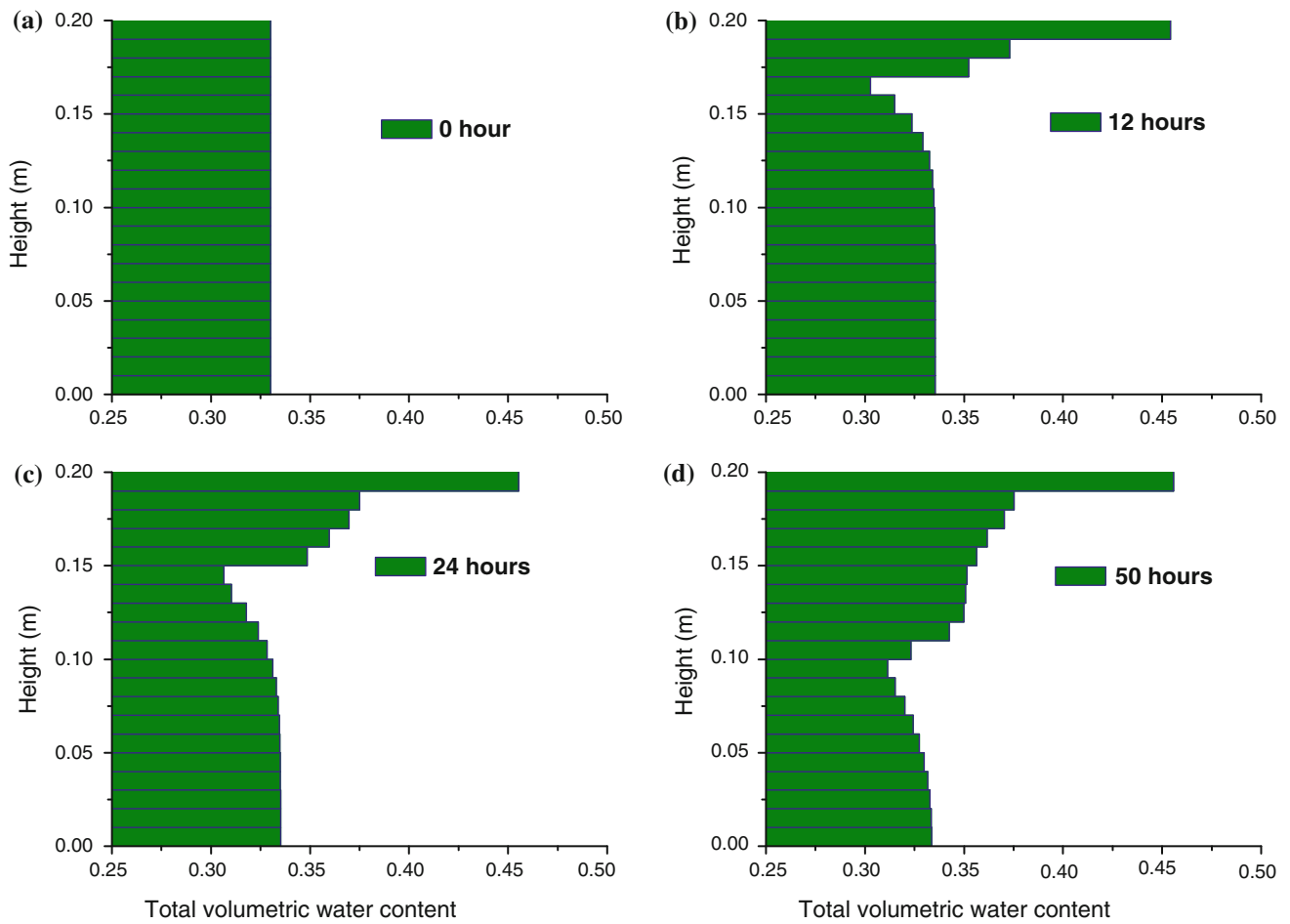


**Fig. 6** Distribution of the total volumetric water content at different times

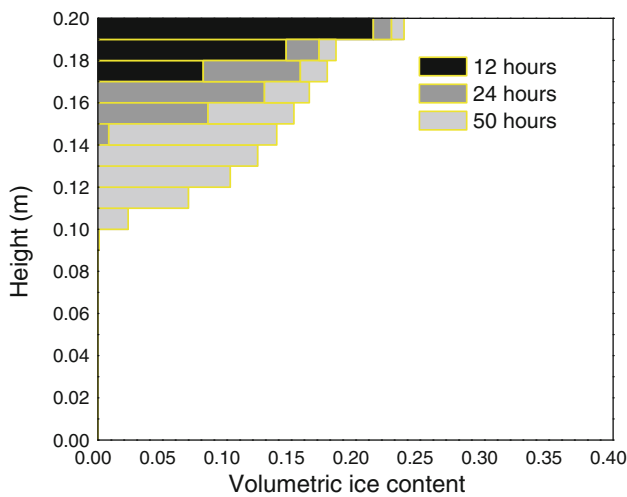


**Fig. 7** The distribution of volumetric ice content at different times

The parameters for model simulation on the effects of thermal conditions on pavement structure are listed in Table 2.

### 7.2 Boundary and initial conditions

Neumann boundary conditions, or heat and fluid flux boundaries, were used for the thermal and hydraulic fields, respectively. A Dirichlet boundary condition was assigned for the mechanical field to ensure the boundaries are either free or fixed in a specific direction. Convective heat transfer was assigned along the boundary exposed to the atmosphere (Eq. 17). Based on the duration of the sunshine and surface wind speed data, a constant coefficient,  $h_c$ , for convective heat transfer was assumed. The  $h_c$  values for pavement and soil surface were assumed to be 25 and 35, respectively, based on typical wind speed data [3]. The influence of short wave and black body radiation was neglected in this study.

The surface water retention can significantly influence the infiltration of water into the pavement base. A conceptual model was formulated for the near-surface water dynamics as following (Eq. 28, [16])

$$\Delta S = P - R - E - T - D \tag{28}$$

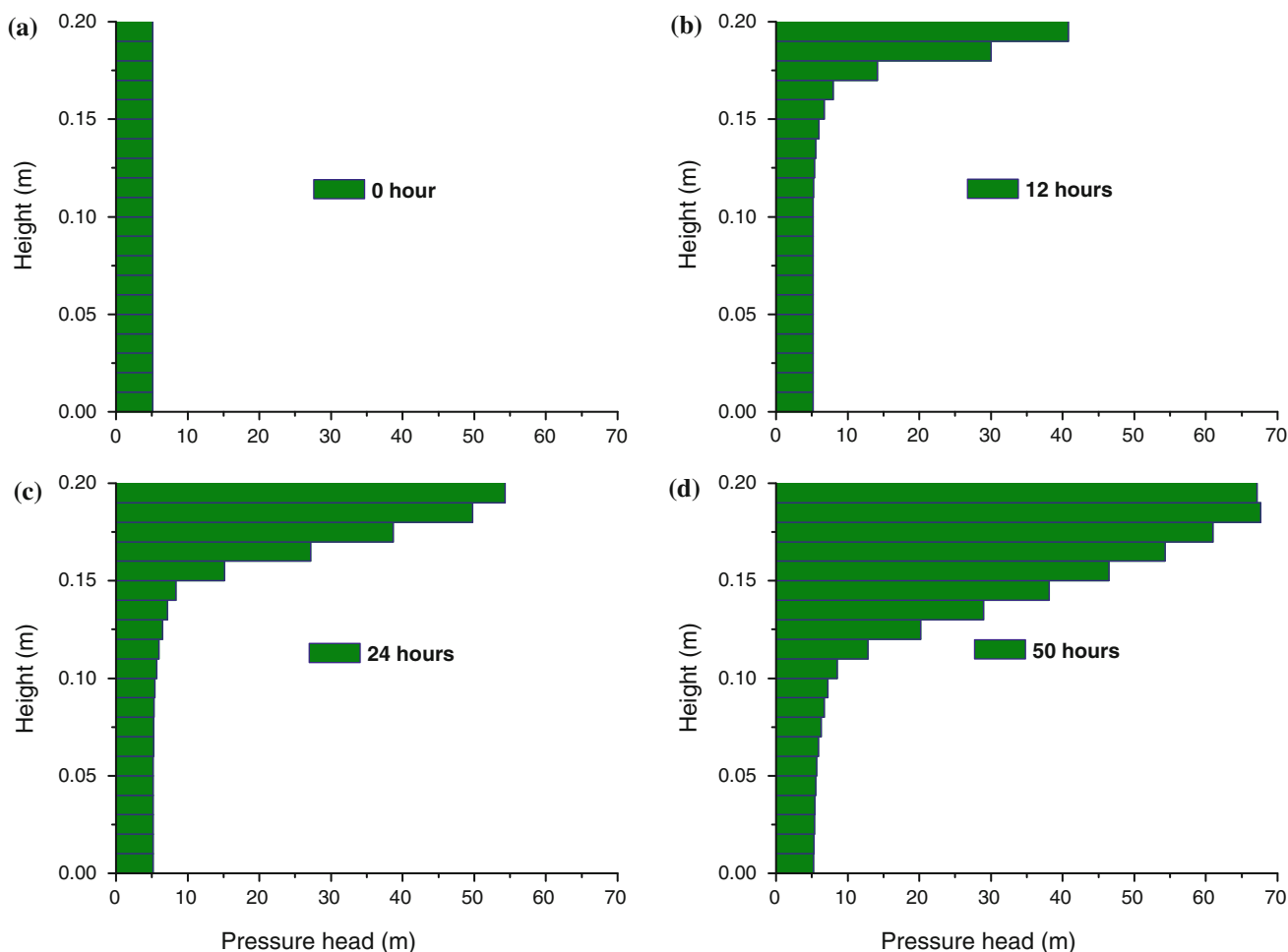


Fig. 8 The vertical distribution of matric potential head (absolute value) at different times

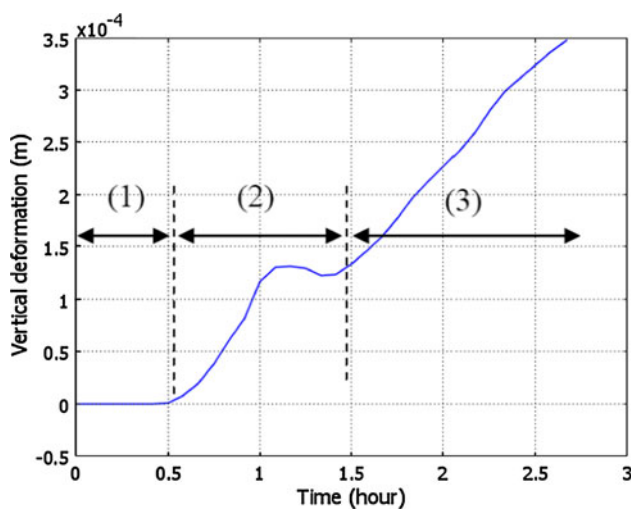


Fig. 9 Total vertical deformation versus time

where  $\Delta S$  is the change in soil water storage,  $P$  is the precipitation,  $R$  is the amount of water running off,  $E$  is the evaporation,  $T$  is the transpiration of plants, and  $D$  is the

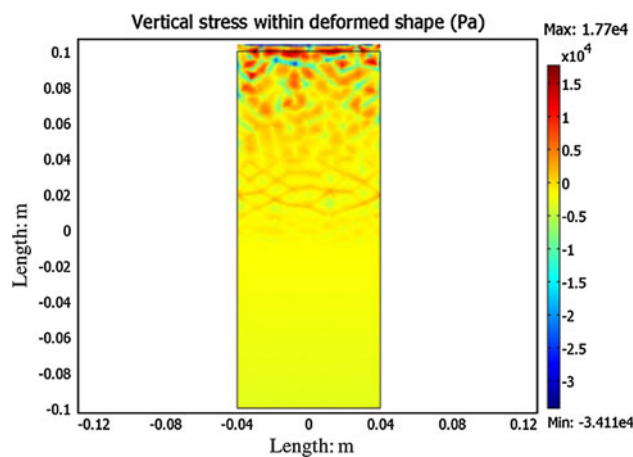
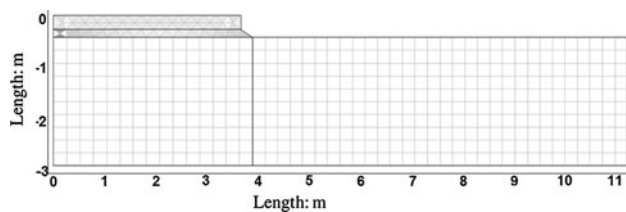


Fig. 10 The distribution of internal stress under freezing effects

drainage. In this case study,  $T$  was neglected and  $E$  was assumed to be  $2.25 \times 10^{-8}$  m/s (Delaware County Water Resources).

For the upper boundary of the subgrade, 6% of the precipitation is entered as the influx that can affect the



**Fig. 11** Meshed computational domain and boundary

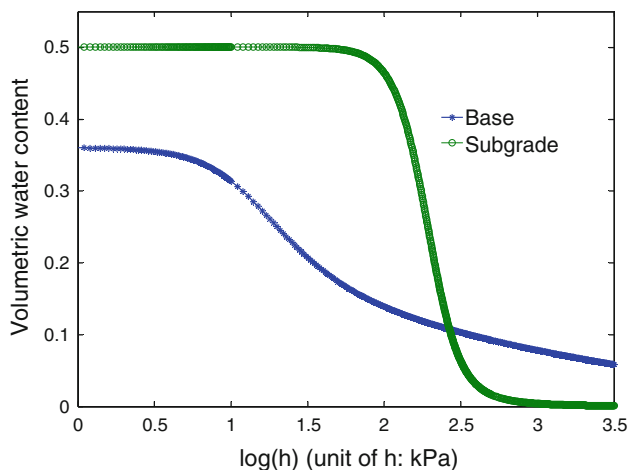


**Fig. 12** Soil water characteristic curves of base and subgrade

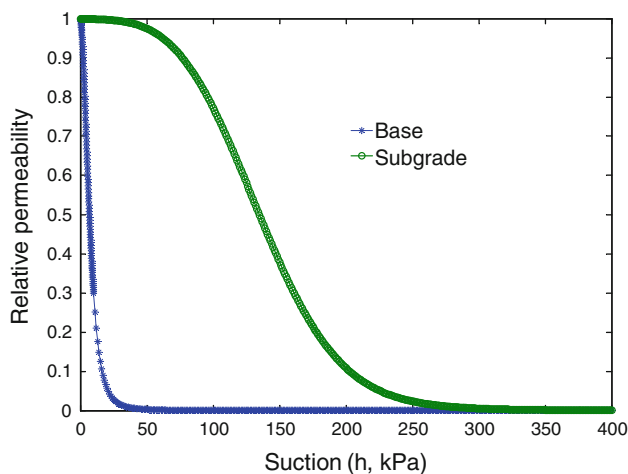


**Fig. 13** Hydraulic conductivity versus suction in base and subgrade

moisture variation of subgrade soil according to local statistics (Delaware County Water Resources). Other than evaporation, water influx into base was controlled by both the cracks and openings of the pavement and the amount of the precipitation. For all the upper boundaries, infiltration was maintained to cease as the matric potential is equal to zero when full saturation is reached. The depth of water table increased from 9.8 feet to 10 feet, an equivalent

downward flux of  $3.5 \times 10^{-8}$  m/s as drainage was assigned on the bottom of the computational domain.

The initial temperature and hydraulic field were determined by interpolating field-monitoring data. They were then assigned to the model. The data of air temperature variations and precipitation were applied to the surface boundaries during the model simulation.

## 8 Results

Figure 14 illustrates the comparison between measured and simulated temperature variation with time at gauge locations S1, S2, and S5. These temperature gauges were buried 1 inch, 4 inches, and 13 inches under the pavement structure, respectively. As can be seen, the trend of temperature variations predicted by the simulation model matches the trend of measured temperature variation at different depths. In fact, temperature fluctuation close to the surface of pavement structure is most difficult to predict, because thermal conductivity was higher for pavement and the effect of the phase change of water on the energy field is more significant there. It is encouraging that our model simulation reasonably captures the trend of thermal field variations close to the surface of pavement structure. Using the measured temperature as the ‘true’ value, the mean absolute deviation by the model simulation is around  $1.1^\circ\text{C}$  and the root mean square of error is around  $1.5^\circ\text{C}$ . Potential sources of error include overlooking the effects of solar radiation and wind and approximation of the initial temperature and water distributions.

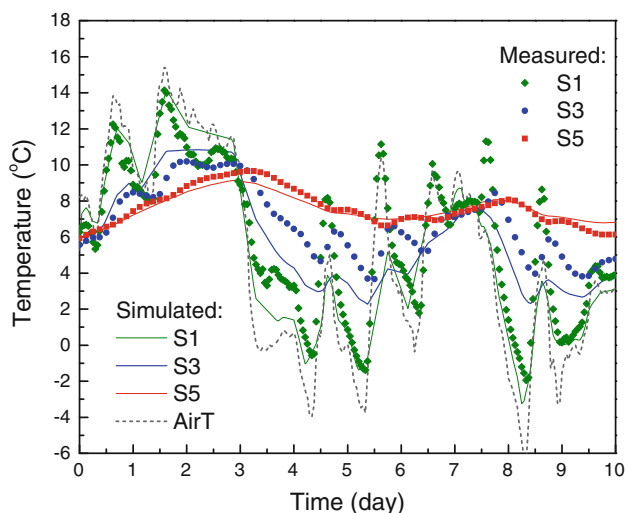
In Fig. 15, the simulated results of temperature distribution versus depth at 0, 5, and 9 days were plotted. The measured temperature distributions with 18 gauges were also plotted. Simulated results agree very well with the field measured data. The difference of predicted temperature is typically within  $\pm 1^\circ\text{C}$  of measured temperature at most locations. The mean absolute deviation of model simulation results is around  $0.3^\circ\text{C}$ , and the root mean square of error is around  $0.4^\circ\text{C}$ .

Figure 16 shows the comparison of simulated and measured moisture content distribution at different times. The predicted moisture content distribution matches the field measured trend. It is noticed that the level of errors is slightly larger for the predicted moisture content in the base layer. This is possibly due to the large variation of the hydraulic conductivity at the interface between base and subgrade materials. With exception of the pavement–subgrade interface, the model simulation achieved a mean absolute deviation of around  $0.009 \text{ m}^3/\text{m}^3$  and root mean square of error of  $0.016 \text{ m}^3/\text{m}^3$ . This accuracy is better compared with commonly used uncoupled models

**Table 2** Parameters for model simulation of pavement structure

Constant	Value	Units	Description
$\theta_{s1}$	0.05	1	Saturated water content of base
$\theta_{s2}$	0.535	1	Saturated water content of subgrade
$K_{s1}$	$8.467 \times 10^{-4}$	m/s	Saturated hydraulic conductivity of base
$K_{s2}$	$8.467 \times 10^{-10}$	m/s	Saturated hydraulic conductivity of subgrade
$n_1$	0.3	1	Porosity of base
$n_1$	0.4	1	Porosity of subgrade
$\lambda_p$	1.3	W/m K	Thermal conductivity of asphalt pavement
$C_{pp}$	$2 \times 10^{-6}$	J/(m <sup>3</sup> K)	Volumetric heat capacity of asphalt pavement

See Table 1 for other parameters



**Fig. 14** Simulated and measure temperature varies with time

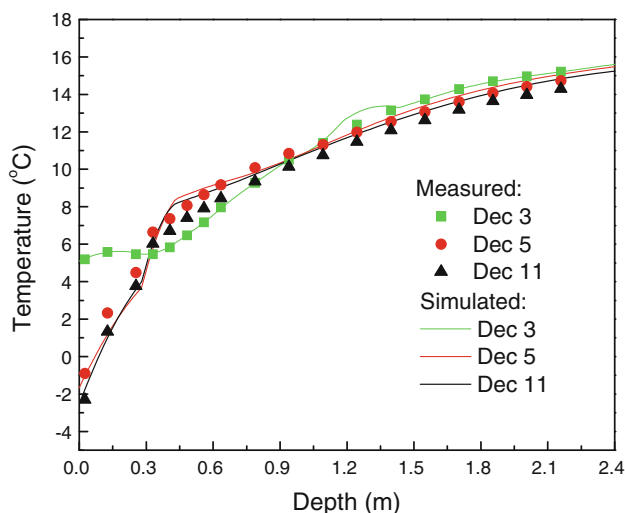


**Fig. 15** Simulated and measure temperature distributions

such as the Enhanced Integrated Climate Model (EICM, [65]). The model can be used to study the performance of pavement under different climate conditions, such as the

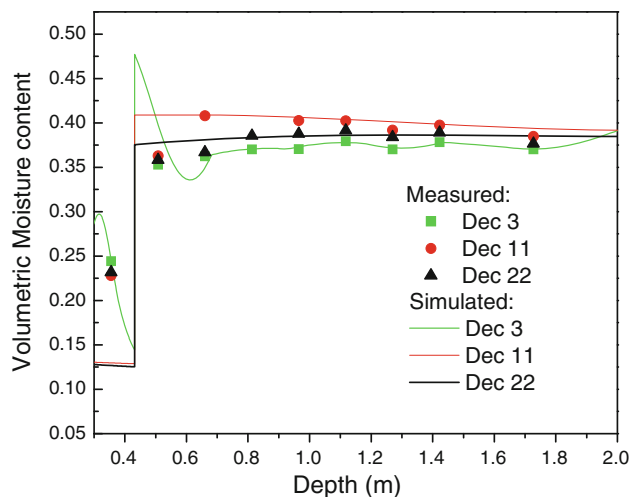


**Fig. 16** Simulated and measured moisture content distributions

seasonal variations of resilient moduli, which are important for the durability of pavement [65].

### 9 Conclusions

A theoretical framework for multiphysics simulations of freezing porous materials is presented in this paper. The thermal, hydraulic, and mechanical fields were coupled together via partial differential equations. The effects of pores on individual physical processes were described by the SWCC and the Clapeyron equation. The highly nonlinear system was solved numerically in a multi-physical simulation platform. The following observations can be made from the simulation results. (1) The thermal-hydro-mechanical fields are strongly coupled in porous materials. Heat transfer induces change in the hydraulic and a stress field, the process is especially important when phase change of pore solutions is involved. (2) Matric potential in unsaturated porous media can cause the volume change pattern that is

different solely due to ice formation. (3) Multiphysical simulation described reasonably well the temperature and moisture variations observed under an in-service pavement.

**Acknowledgments** The authors gratefully acknowledge the help and support from the Ohio Department of Transportation and the Cleveland Water Division during the course of this study. The financial support of this study is partially from NSF project CMMI 0856407.

## References

- Anderson DM, Tice AR, McKim HL (1973) The unfrozen water and the apparent specific heat capacity of frozen soils. In: Proceedings of the second international conference on permafrost; North American contribution. Natl Acad Sci, Washington, DC, pp 289–295
- Bai M, Elsworth D (2000) Coupled processes in subsurface deformation, flow and transport. ASCE Press, Reston
- Bentz DP (2000) A computer model to predict the surface temperature and time-of-wetness of concrete pavements and bridge decks. NISTIR 6551, U.S. Department of Commerce
- Biot MA (1941) General theory of three-dimensional consolidation. *J Appl Phys* 12(2):155–164
- Campbell GS (1985) Soil physics with BASIC: transport models for soil-plant systems. Elsevier, Amsterdam
- Cary JW (1965) Water flux in moist soil: thermal versus suction gradients. *Soil Sci* 100(3):168–175
- Cary JW (1966) Soil moisture transport due to thermal gradients: practical aspects. *Soil Sci Soc Am Proc* 30(4):428–433
- Cass AG, Campbell GS, Jones TL (1981) Hydraulic and thermal properties of soil samples from the buried waste test facility. PNL-4015, Pacific Northwest Laboratory, Richland
- Celia MA, Binning P (1992) A mass conservative numerical solution for two-phase flow in porous media with application to unsaturated flow. *Water Resour Res* 28:2819–2828
- Celia MA, Bouloutas EF, Zarba RL (1990) A general mass-conservative numerical solution for the unsaturated flow equation. *Water Resour Res* 26(7):1483–1496
- Chen JS, Lin KY, Young SY (2004) Effects of crack with permeability on moisture-induced damage of pavement. *J Mater Civil Eng* 16(3):276–282
- Childs EC, Collis-George GN (1950) The permeability of porous materials. *Proc R Soc Lond A* 201:392–405
- Coussy O (2005) Poromechanics. Wiley, Chichester
- Coussy O, Monteiro P (2007) Unsaturated poroelasticity for crystallization in pores. *Comput Geotech* 34:279–290
- Dash JG (1989) Thermomolecular pressure in surface melting: motivation for frost heave. *Science* 246:591–593
- Fayer MJ (2000) UNSAT-H version 3.0: unsaturated soil water and heat flow model, theory, user manual, and examples, Report 13249, Pac. Northwest Natl. Lab, Richland
- Fredlund DG, Rahardjo H (1993) Soil mechanics for unsaturated soils. Wiley, New York
- Fredlund DG, Xing A (1994) Equations for the soil-water characteristic curve. *Can Geotech J* 31:521–532
- Fredlund DG, Xing A, Huang S (1994) Predicting the permeability function for unsaturated soils using the soil-water characteristic curve. *Can Geotech J* 31:533–546
- Gardner WR (1958) Some steady-state solutions of the unsaturated moisture flow equation with application to evaporation from a water table. *Soil Sci* 85:228–232
- Gilpin RR (1980) A model for the prediction of ice lensing and frost heave in soils. *Water Resour Res* 16:918–930
- Guymon GL, Luthin JN (1974) A coupled heat and moisture transport model for arctic soils. *Water Resour Res* 10(5):995–1001
- Hansson K, Simunek J, Mizoguchi M et al (2004) Water flow and heat transport in frozen soil: numerical solution and freeze-thaw applications. *Vadose Zone J* 3:693–704
- Harlan RL (1973) Analysis of coupled heat-fluid transport in partially frozen soil. *Water Resour Res* 9:1314–1323
- Heydinger AG (2003) Monitoring seasonal instrumentation and modeling climatic effects on pavements at the Ohio-SHRP test road, Report No. FHWA/OH-2003/018
- Horiguchi K, Miller RD (1980) Experimental studies with frozen soil in an “ice sandwich” permeameter. *Cold Regions Sci Technol* 3:177–183
- Jame YW, Norum DI (1980) Heat and mass transfer in a freezing unsaturated porous medium. *Water Resour Res* 16(4):811–819
- Konrad JM (1994) Sixteenth Canadian geotechnical colloquium-frost heave in soils: concepts and engineering. *Can Geotech J* 31(2):223–245
- Konrad JM, Morgenstern NR (1981) The segregation potential of a freezing soil. *Can Geotech J* 18:482–491
- Koopmans RWR (1966) Soil freezing and soil water characteristic curves. *Soil Sci Soc Am Proc* 30(6):680–685
- Liu Y, Yu XB, Yu X (2009) Measurement of soil air suction change during freeze-thaw process with the aid of an innovative time domain reflectometry sensor. *Can Geotech J* (under review)
- Lundin LC (1989) Water and heat flows in frozen soils. Basic theory and operational modeling. Ph.D. Thesis, Uppsala University, Uppsala, Sweden
- Masada T, Sargand SM (2001) Laboratory characterization of materials & data management for Ohio-SHRP projects (U.S. 23), Report No. FHWA/OH-2001/07
- McInnes KJ (1981) Thermal conductivities of soils from dryland wheat regions of Eastern Washington. M.S. Thesis, Washington State University, Pullman
- Miller RD (1978) Frost heaving in non-colloidal soils. In: Proceedings third international permafrost conference, Edmonton, Canada, pp 708–713
- Mizoguchi M (1990) Water heat and salt transport in freezing soil. Ph. D. Thesis, University of Tokyo
- Mizoguchi M (1993) A derivation of matric potential in frozen soil. Bulletin of the Faculty of Bioresources, Mie University, Tsu, Japan, no 10, pp 175–182
- Mualem Y (1986) Hydraulic conductivity of unsaturated soils: prediction and formulas. Methods of soil analysis, part I, 2nd edn. In: Klute A (ed) Agronomy monographs, no 9. ASA and SSSA, Madison, pp 799–823
- Newman GP, Wilson GW (1997) Heat and mass transfer in unsaturated soils during freezing. *Can Geotech J* 34:63–70
- Nishimura S, Gens A, Olivella S, Jardine RJ (2009) THM-coupled finite element analysis of frozen soil: formulation and application. *Geotechnique* 59(3):159–171
- Nixon JF (1992) Discrete ice lens theory for frost heave beneath pipelines. *Can Geotech J* 29(3):487–497
- Noborio K, McInnes KJ, Heilman JL (1996) Two-dimensional model for water, heat and solute transport in furrow-irrigated soil: I. Theory. *Soil Sci Soc Am Proc* 60:1001–1009
- Noborio K, McInnes KJ, Heilman JL (1996) Two-dimensional model for water, heat, and solute transport in furrow-irrigated soil: II. Field evaluation. *Soil Sci Soc Am J* 60:1010–1021
- Noorishad J, Tsang CF, Witherspoon PA (1992) Theoretical and field studies of coupled hydromechanical behaviour of fractured rocks-I: development and verification of a numerical simulator. *Int J Rock Mech Mining Sci* 29(4):401–409

45. O'Neill K, Miller RD (1985) Exploration of a rigid ice model of frost heave. *Water Resour Res* 21(3):281–296
46. Philip JR, de Vries DA (1957) Moisture movement in porous materials under temperature gradients. *Eos Trans Am Geophys Union* 38:222–232
47. Reeves PC, Celia MA (1996) Functional relationships between capillary pressure, saturation, and interfacial area as revealed by a pore-scale network model. *Water Resour Res* 32:2345–2358
48. Rowe RK (2001) *Geotechnical and geoenvironmental engineering handbook*. Kluwer, Massachusetts
49. Rutqvist J, Börgesson L, Chijimatsu M et al. (2001) Thermo-hydro-mechanics of partially saturated geological media: governing equations and formulation of four finite element models. *Int J Rock Mech Mining Sci* 38(1):105–127
50. Sahimi M (1995) Flow and transport in porous media and fractured rock. VCH, Weinheim
51. Sawada S (1977) Temperature dependence of thermal conductivity of frozen soil. Research Report of Kitami Institute of Technology
52. Schofield RK (1935) The pF of the water in soil. In: *Transactions 3rd international congress of soil science*, vol 2, no 22, pp 37–48
53. Shao J (1994) A surface-temperature prediction model for porous asphalt pavement and its validation. *Meteorol Appl* 1(2):89–98
54. Sheng D, Axelsson K, Knutsson S (1995) Frost heave due to ice lens formation in freezing soils I. Theory and verification. *Nordic Hydrol* 26(2):125–146
55. Simonsen E, Janoo VC (1997) Prediction of temperature and moisture changes in pavement structures. *J Cold Regions Eng* 11(4):291–307
56. Simunek J, Sejna M, van Genuchten MT (1998) *The Hydrus-1D software package for simulating the one-dimensional movement of water, heat, and multiple solutes in variably-saturated media, user's manual, version 2.0*, U.S. Salinity Lab., Agricultural Research Service, Riverside
57. Spaans M (1996) Monte Carlo models of the physical and chemical properties of inhomogeneous interstellar clouds. *Astron Astrophys* 307:271–287
58. Stephansson O, Jing L, Tsang CF (1996) *Coupled thermo-hydro-mechanical processes of fractured media*. Elsevier, Rotterdam
59. Thomas HR, He Y (1995) Analysis of coupled heat, moisture and air transfer in a deformable unsaturated soil. *Geotechnique* 45(4):677–689
60. Thomas HR, He Y (1997) A coupled heat-moisture transfer theory for deformable unsaturated soil and its algorithmic implementation. *Int J Numer Methods Eng* 40:3421–3441
61. Thomas HR, King SD (1991) Coupled temperature/capillary potential variations in unsaturated soil. *J Eng Mech* 117(11):2475–2491
62. Thomas HR, Cleall P, Li YC et al (2009) Modelling of cryogenic processes in permafrost and seasonally frozen soils. *Geotechnique* 59(3):173–184
63. van Genuchten MT (1980) A close-form equation for predicting the hydraulic conductivity of unsaturated soil. *Soil Sci Soc Am J* 44(5):892–898
64. Watanabe K, Wake T (2008) Capillary bundle model of hydraulic conductivity for frozen soil. *Water Resour Res* 44:1927–1932
65. Wolfe WE, Butalia TS (2004) Seasonal instrumentation of SHRP pavement. Report No. FHWA/OH-2004/007
66. Delaware County Water Resources. [http://ohioline.osu.edu/aex-fact/0480\\_21.html](http://ohioline.osu.edu/aex-fact/0480_21.html)
67. Yavuzturk C, Ksaibati K (2002) Assessment of fluctuations in asphalt pavement due to thermal environmental conditions using a two-dimensional transient finite differential approach. Department of Civil and Architectural Engineering, University of Wyoming, Wyoming
68. Yuan D, Nazarian S (2004) Variation in moduli of base and subgrade with moisture. In: *Transportation Research Board 82nd Annual Meeting*, 2003
69. Zapata CE, Houston WN, Houston SL et al. (2000) Soil water characteristic curve variability. *Adv Unsatur Geotech* 84–123